DOI: 10.1002/((please add manuscript number))
Article type: Full Paper

Phosphorus Regulated Cobalt Oxide@Nitrogen-Doped Carbon Nanowires for Flexible Quasi-Solid-State Supercapacitors

Shude Liu,[1] Ying Yin,[1, 2] Yang Shen,[3] Kwan San Hui,[4] Young Tea Chun,[5] Jong Min Kim,[5] Kwun Nam Hui,*[,6] Lipeng Zhang,*[,3] and Seong Chan Jun*[,1]

[1]School of Mechanical Engineering, Yonsei University, Seoul 120-749, South Korea.
[2]Guangxi Key Laboratory of Information Materials, Guilin University of Electronic Technology, Guilin 541004, PR China.
[3]College of Chemical Engineering, Beijing University of Chemical Technology, Beijing, 100029 China.
[4]School of Engineering, University of East Anglia, Norwich, NR4 7TJ, United Kingdom.
[5]Department of Engineering, University of Cambridge, 9 JJ Thomson Avenue, Cambridge 01223, UK
[6]Institute of Applied Physics and Materials Engineering, University of Macau, Avenida da Universidade, Taipa, Macau, China.
*Corresponding author's E-mail: bizhui@umac.mo; zhanglipeng2011@gmail.com; scj@yonsei.ac.kr

Keywords: in situ structural reconstruction, orientated metal organic framework, anion regulation, encapsulated hybrid, flexible quasi-solid-state supercapacitors

Abstract

Battery-type materials are promising candidates to achieve high specific capacity for supercapacitors. However, their slow reaction kinetics hinders the improvement in electrochemical performance. Herein, we report a hybrid structure of P-doped Co_3O_4 (P-Co_3O_4) ultrafine nanoparticles in situ encapsulated into P, N co-doped carbon (P, N-C) nanowires by a pyrolysis-oxidation-phosphorization of 1D metal–organic framework derived from Co-layered double hydroxide as self-template and reactant.

This hybrid structure prevents active material agglomeration and maintains a 1D oriented arrangement, which exhibits a large accessible surface area and hierarchically porous feature, enabling sufficient permeation and transfer of electrolyte ions. Theoretical calculations demonstrate that the P dopants in P-Co_3O_4@P, N-C could reduce the adsorption energy of OH^- and regulate the electrical properties. Accordingly, the P-Co_3O_4@P, N-C delivers a high specific capacity of 669 mC cm^{-2} at 1 mA cm^{-2} and an ultralong cycle life with only 4.8% loss over 5000 cycles at 30 mA cm^{-2}. During the fabrication of P-Co_3O_4@P, N-C, Co@P, N-C is simultaneously developed, which can be integrated with P-Co_3O_4@P, N-C for the assembly of asymmetric supercapacitors. These devices achieve a high energy density of 47.6 W h kg^{-1} at 750 W kg^{-1} and impressive flexibility, exhibiting a great potential in practical application.

1. Introduction

The ever-increasing popularity of portable and flexible electronics has stimulated extensive research on efficient energy-storage technologies.[1] As newly developed energy supply systems, flexible supercapacitors have captured extensive interest due to their advantageous features of high mechanical bendability, fast charge/discharge capability, and high power density.[2] Specifically, solid-state supercapacitors are gaining increased attention because they avoid the electrolyte leakage that occurs in traditional aqueous electrolyte-based ones.[3] However, the attained energy density of most developed flexible solid-state supercapacitors remains lower than that of lithium-ion batteries,[1a, 4] severely hindering the application potential of these supercapacitors

for powering flexible energy-consuming systems. Generally, supercapacitors with battery-type materials have high specific capacity but still suffer from inferior rate performance and poor cyclic stability due to the slow ionic diffusion and sluggish electron transfer kinetics of the electrode materials upon cycling.[5] Accordingly, reduction of their particle size, increase of their electroactive surface area, combination with conductive carbon and/or development of surface defect engineering have been well-recognized to potentially transform battery-type materials into "extrinsic" pseudocapacitive materials. Consequently, more charge storage can occur at or near the surface region of the electrodes for pseudocapacitance,[6] ensuring the large charge proportions for the capacitive process of such electrode materials.

In this regard, some strategies to develop intriguing structures have been proposed. As shown in **Figure 1**, for strategy 1, the bulk structured electroactive species are deposited directly on a conductive substrate without using polymer binder and conductive additives, which can eliminate the "dead surface" of the electrode and facilitate effective electron transport.[7] However, the ionic diffusion within the bulk material is still sluggish to a certain extent due to fewer voids and spaces within the electrode material, thereby degrading ion-transport rate. Substantial efforts have been adopted to various electroactive nanostructures integrated on conductive substrate (strategy 2)[6e, 8] to provide an efficient pathway for electron transfer and shorten diffusion paths for ion transport.[7b] Unfortunately, the intrinsically poor electronic conductivity of battery-type materials impedes electron transportation, leading to degraded electrochemical

stability during cycling.[9] The use of a hybrid electrode with nanosized active material coated with a highly conductive carbon would be an effective approach to improve electrical properties (strategy 3).[10] However, such battery-type materials/surface carbon hybrids still cannot fully expose the reactive sites, hindering electrolyte penetration and access to the electrochemically active sites of the electrode materials. Accordingly, self-template-assisted synthesis of metal-organic-frameworks (MOFs) from oriented-grown layered double hydroxides (LDHs) on conductive support has been demonstrated to effectively address the agglomeration of MOF particles during pyrolysis while providing an oriented arrangement of MOFs.[2f, 11] For this purpose, we propose an innovative strategy to rationally design the MOF-derived hybrid with ultrafine electroactive species embedded within carbon matrix (strategy 4). In this configuration, the in situ-decorated metal oxides are fully enwrapped in MOF-derived porous carbon that provide strong bridged bonds, enabling fast electron/charge transfer kinetics,[12] which are not exhibited by conventional planar integrated hybrids.[13]

Meanwhile, the electrochemical kinetics of transition metal oxides can be enhanced through anion doping.[14] For example, Yu and co-workers reported that the introduction of N atoms into the parent Co_3O_4 induced charge redistribution, which is favorable for enhanced electronic conductivity, increased O_2 adsorption strength, and improved catalytic activity of oxygen reduction reaction.[15] Zhang and co-workers stated that the partial substitution of P anions at the O sites of Fe_2O_3 greatly regulates covalent bonds, offering more carriers and reducing the energy required to drive the photo-

electrochemical processes.[16] Furthermore, anion doping of carbon materials has demonstrated as an effective approach for enhanced electrochemical properties owing to the tailoring of the electronic structure and effects on the electronic charge distribution of adjacent carbon atoms.[17] With the above considerations in mind, it is highly desirable to develop an anion doping in metal oxide and carbon derived from structural oriented-grown MOF on conductive substrate carbon cloth (CF) to fully improve the electrochemical performance in supercapacitors, which has yet to be reported.

Herein, we propose an in situ structural reconstruction strategy to synthesize oriented Co−MOF nanowires on CF substrate using Co−LDH as both precursor and self-sacrificing template. After a pyrolysis−oxidation−phosphorization treatment, the Co−MOF is converted into P-Co_3O_4@P, N-C with ultrafine P-Co_3O_4 particles in situ embedded into P, N-C nanowires. This hybrid structure provides strong intercomponent synergy, increases availability of active sites/interfaces and improves the electron/ion transfer, giving rise to high electrochemical reactivity. Density functional theory calculations reveal that the incorporated P atoms in P-Co_3O_4 and P, N-C tune their electronic structure and decrease adsorption barrier of OH^- at the active sites, thereby further facilitating the electrochemical reaction kinetics of P-Co_3O_4@P, N-C. As a result, the hybrid electrode exhibits a superior specific capacity of 669 mC cm^{-2} at 1 mA cm^{-2}, good rate capability (76.7% capacity retention at 30 mA cm^{-2}), and excellent cycling performance with a capacity retention of 95.2% after 5000 cycles. During the synthesis

of P-Co_3O_4@P, N-C, Co@P, N-C is simultaneously obtained, which can be served as negative electrode coupling with P-Co_3O_4@P, N-C positive electrode for assembling flexible asymmetric supercapacitors (ASCs). The ASC devices achieve appreciable energy and power density of 47.6 W h kg^{-1} and 750 W kg^{-1}, respectively, as well as considerable mechanical flexibility with an essentially unchanged capacitance in different bending states. It is anticipated that this work provides a promising design route for the next generation of high performance electrode materials.

2. Results and discussion

2.1 Synthesis of electrode materials

Figure 2 illustrates the synthesis of P-Co_3O_4@P, N-C and Co@P, N-C nanowires on CF substrate. Initially, wire-like cobalt chloride carbonate hydroxide arrays (denoted as Co−LDH) are grown on CF substrate through a hydrothermal method, as observed by field-emission scanning electron microscopy (FESEM) in Figure S1a−c. All the diffraction peaks of Co−LDH can be indexed to crystalline LDH phase (JCPDS No. 38-0547; Figure S1d).[18] Afterwards, the obtained Co−LDH is employed as self-sacrificial template to generate Co^{2+} ions and a skeleton for the in situ growth of Co−MOF (Figure S2). Specifically, Co−LDH possesses a typical layered structure in which the interlayer anions between 2D host layers allow the free diffusion of H^+ ions and 2-methylimidazole (HMe-Im) molecules. Further, Co−LDH, which is a mild base, deprotonates HMe-Im with the assistance of water solvent,[19] leading to the breakage of Co–OH bonds and the formation of deprotonated HMe-Im species (Me-Im). The

dissociative Co^{2+} then coordinates with Me-Im linkers via in situ structural reconstruction process, leading to the formation of Co(Me-Im) nanonuclei. As the reaction proceeded, the generated crystal nuclei tends to aggregate directionally to reduce the interfacial energy and then gradually forms Co(Me-Im) nanowires due to the 1D nature of the template. The recorded XRD pattern of Co(Me-Im), shown in Figure S3a, is in good agreement with the reported crystallographic structure of Co–MOF (ZIF–67),[20] demonstrating a complete phase conversion from Co−LDH to Co–MOF. The FESEM images of Co–MOF reveals that the nanowire morphology can be retained but with very rough surface (Figure S3b), which is caused by the ion exchange/etching process at the interface between the newly formed Co–MOF and Co−LDH. Correspondingly, the color of the sample ranges from pink to purple after the in situ structural reconstruction process (Insets in Figures S1d and S3a). To verify the universality of this synthesis strategy, MCo−LDHs (Ni, Cu and Zn) are also used as templates for the construction of MCo−MOFs (Ni, Cu and Zn) with similar coordination modes (Figure S4). Analogous to Co−MOF, MCo−MOFs also inherit intrinsic structure feature of the MCo−LDHs precursors, and their cross-linked nanostructures are vertically aligned along the axial direction of the whole CF skeleton (Figure S5). A color variation from pink to purple is observed from a series of samples synthesized after the evolution from LDHs to MOFs (Figure S6). To further clarify the occurrence of phase transformation, we recorded EDS mappings from the coordinated MCo−MOFs (Figures S7–S9). These results disclose that M, Co, C, and N are distributed homogeneously in their corresponding MCo−MOFs structures, revealing

the successful coordination between MCo species and Me-Im ligand. Subsequent pyrolysis of Co−MOF nanowires at 600 °C under Ar atmosphere leads to the formation of Co/N-doped C (Co@N-C; black color), as presented in Figure S10. During the process, the Co^{2+} ions in Co−MOF are reduced into Co nanoparticles, whereas the coordinated organic ligands from Co−MOF are transformed into 1D N-doped carbon nanostructures, which can be confirmed by XRD pattern (Figure S11). After subsequent low-temperature oxidation under air and phosphorization in flowing Ar, the Co@N-C nanowires are converted into Co_3O_4/N-doped C (Co_3O_4@N-C) and P-Co_3O_4@P, N-C, respectively. The Co@N-C nanowires are then subjected to the subsequent phosphorization at 300 °C in Ar atmosphere to generate the Co@P, N-C.

2.2 Characterization and charge storage properties of positive electrode materials

Figures 3a, b and S12 show the typical SEM images of the as-obtained P-Co_3O_4@P, N-C nanowires with diameter of ~200 nm, which are aligned and densely grown on the surface of CF substrate. In comparison with the Co@N-C, there is no obvious morphological change in the P-Co_3O_4@P, N-C structure. The energy-dispersive spectrum (EDS) mapping of the P-Co_3O_4@P, N-C clearly identifies the existence of P, Co, O, N, and C (Figure S13). More details about the P-Co_3O_4@P, N-C nanocomposite were investigated by transmission electron microscopy (TEM). Figure 3c, d clearly reveal that numerous small P-Co_3O_4 nanoparticles with dark contrast (15~30 nm) are imbedded in the 1D graphitic carbon matrix. Clearly, the nanowires display a porous character, which can be ascribed to the released gases and created pores as a result of

the decomposition of organic ligands. As observed in the N_2 adsorption−desorption curves (Figure S14), all samples show the type IV isotherm with H3 hysteresis loop, suggesting the coexistence of the mesoporous and macroporous features in the samples.[21] Notably, the P-Co_3O_4@P, N-C presents a Brunauer-Emmett-Teller (BET) specific surface area of 97.6 m^2 g^{-1}, which is higher than those of Co_3O_4 (54.7 m^2 g^{-1}), P-Co_3O_4 (66.9 m^2 g^{-1}), and Co_3O_4@N-C (82.5 m^2 g^{-1}). The pore size distribution reveals that the Co_3O_4@N-C possesses larger average pore size (~4.40 nm) than Co_3O_4 (~3.72 nm), whereas the pore size of Co_3O_4@N-C is similar to that of P-Co_3O_4@P, N-C (~4.43 nm), suggesting that the structural reconstruction from LDH to MOF contributes to the increase in pore size. The high surface area with rich hierarchical pores for P-Co_3O_4@P, N-C would provide highly exposed active sites and reduce the diffusion distance of electrolyte ions during the charge–discharge process, which is responsible for enhanced charge storage capacity. High-resolution TEM (HRTEM) image shows two interplanar spacings of 0.286 and 0.247 nm, which can be assigned to the spacings of the (220) and (311) planes of Co_3O_4, respectively (Figure 3e). This finding is consistent with the corresponding SAED pattern (Figure 3f). However, the lattice stripes in the region of aqua dotted line are not obvious, which is due to the generation of disorders and defects within P-Co_3O_4@P, N-C. The scanning TEM (STEM) images and corresponding elemental mappings show that Co, O, C, P, and N are uniformly distributed over the entire nanowire (Figure 3g–m), again confirming that P-Co_3O_4 nanoparticles are successfully in situ encapsulated in the carbon matrix. Thermogravimetric analysis (TGA) result shows that the mass content of carbon in the

P-Co_3O_4@P, N-C is ~22.6 wt% (Figure S15). The carbonaceous content is favorable for improving the electronic conductivity of P-Co_3O_4@P, N-C as confirmed by EIS measurement in Figure S16.

To make a systematic comparison, we prepared Co_3O_4 and P-Co_3O_4 nanowires without in situ structural reconstruction process from Co−LDH by thermally oxidation and subsequent phosphorization, respectively (details shown in experimental section and Figure S17). As observed in **Figure 4**a, the diffraction peaks of Co_3O_4 and P-Co_3O_4 both match well with the pure cubic Co_3O_4 phase,[22] confirming the absence of new phases during phosphorization. Notably, some peaks for P-Co_3O_4 disappear, which is probably due to the degradation of crystallinity.[23] By contrast, Co_3O_4@N-C and P-Co_3O_4@P, N-C powders exhibit another two prominent diffraction peaks at 26.2° and 43.0°, which can be attributed to the (002) and (110) planes of disordered carbonaceous structure.[17b] Apparently, the (311) diffraction peak positions of P-Co_3O_4 and P-Co_3O_4@P, N-C shift to a lower diffraction angle after phosphorization (Figure 4b), which is due to the larger atomic size of P than that of O. The bond structures of the as-prepared samples were investigated by Raman spectroscopy. The Raman spectra of pristine Co_3O_4 and P-Co_3O_4 present four characteristic bands at 481, 520, 619, and 685 cm^{-1} (Figure S18), which can be assigned to the E_g, F_{2g}^1, F_{2g}^2, and A_{1g} vibration modes of the crystalline Co_3O_4, respectively.[12, 22] By contrast, the Raman signals of the Co_3O_4@N-C and P-Co_3O_4@P, N-C hybrids exhibit another two peaks located at approximately 1,369 and 1,587 cm^{-1}, corresponding to the D band (structural

disorder/defects) and G band (graphitic structures) of carbonaceous materials, respectively.[17b] The I_D/I_G of the P-Co_3O_4@P, N-C is ~1.25, which is slightly higher than that of the Co_3O_4@N-C (~1.19), implying more structural disorder and defects within P-Co_3O_4@P, N-C.[24]

To detect the electronic state and chemical environment of surface elements, we carried out X-ray photoelectron spectroscopy (XPS). The Co 2p spectra of Co_3O_4 and Co_3O_4@N-C (Figure 4c) show the binding energies of Co $2p_{3/2}$ and Co $2p_{1/2}$ peaks located at 780.1 and 795.5 eV, respectively, along with a pair of shakeup satellites, suggesting the co-existence of Co^{2+} and Co^{3+} in the Co_3O_4.[25] Besides, the deconvoluted peaks in Co 2p region centered at 782.0 and 797.8 eV are assigned to Co^{2+}, whereas the other peaks at 779.6 and 795.1 eV correspond to Co^{3+}.[26] The Co 2p region associated with octahedral sites is obviously shifted to the lower binding energies after phosphorization, indicating the reduced oxidation state of Co, which is due to the increased electron-density localization around the Co atoms.[22, 25, 27] This finding can be explained by the lower electronegativity and electron-withdrawing ability of P compared with O.[28] This phenomenon can be attributed to the fact that the generated PH_3 gas derived from P precursor is employed as a reductant to produce O-deficient Co_3O_4.[28] In terms of thermodynamics, partial oxygen defects are also favorable to filling P and stabilizing oxygen defects.[29] Based on the fitted curve area of Co^{3+} and Co^{2+} in Co 2p region, the molar ratios of Co^{2+}/Co^{3+} for P-Co_3O_4 and P-Co_3O_4@P, N-C are higher than those of Co_3O_4 and Co_3O_4@N-C, implying that a portion

of Co^{3+} on the surface is reduced to Co^{2+} accompanied by the presence of oxygen vacancies, which is consistent with previous reports.[22, 27, 30] The electron paramagnetic resonance (EPR) was performed to investigate the unpaired electrons in the as-synthesized samples.[31] Obviously, the P-Co_3O_4, Co_3O_4@N-C and P-Co_3O_4@P, N-C all show a stronger EPR signal at g = 1.97 than Co_3O_4, and P-Co_3O_4@P, N-C displays the highest EPR signal intensity (Figure S19), which indicates that more the lattice electron trapping sites are generated within P-Co_3O_4@P, N-C.[28, 32] For the N 1s region of Co_3O_4@N-C and P-Co_3O_4@P, N-C (Figure 4d), four separated peaks with binding energies of 398.5, 400.1, 401.2, and 403.1 eV are observed, which could be assigned to pyridinic-N, pyrolic-N, graphitic-N, and oxidized-N groups, respectively.[33] The XPS spectra of P-Co_3O_4 and P-Co_3O_4@P, N-C present a P 2p region that indicates the existence of P on the surface, whereas no P signal is detected in the spectra of Co_3O_4 and Co_3O_4@N-C (Figure 4e). For the P 2p spectrum, two characteristic peaks with binding energies at ~129.8 and 134.2 eV are found, which correspond to negatively charged $P^{\delta-}$ (Co−P) and phosphates, respectively, whereas additional component centered at ~133.2 eV is assigned to P–O–C.[17b] The incorporated P with larger atomic radius than C in the carbon lattice could induce increased structural distortion and produce more defects to increase the amount of active sites in the carbon, thereby enhancing the electrochemical properties. For the O 1s XPS spectrum of Co_3O_4 (Figure 4f), the peak located at ~529.9 eV can be attributed to lattice oxygen (O^{2-}), whereas the other one at ~533.1 eV is indexed to surface-adsorbed H_2O.[26b] The newly formed hump peak at ~531.4 eV for Co_3O_4@N-C confirms the enrichment of defect sites with

low oxygen coordination relative to that in Co_3O_4,[22] whereas the peak at 532.4 eV can be attributed to C–OH/C–O–C.[26a] An additional peak at ~531.8 eV for P-Co_3O_4 and P-Co_3O_4@P, N-C is observed, which can be assigned to phosphate species on the surface during phosphorization treatment.[34]

The electrochemical properties of the as-fabricated samples were evaluated by a three-electrode configuration in 2 M KOH aqueous electrolyte. **Figure 5**a shows the comparison of the cyclic voltammetry (CV) curves of Co_3O_4, P-Co_3O_4, Co_3O_4@N-C, and P-Co_3O_4@P, N-C electrodes at a scan rate of 50 mV s^{-1} with an operating potential of 0–0.45 V versus the saturated calomel electrode (SCE). A pair of redox peaks can be observed in every CV curve, which can be attributed to the Faradaic redox reactions of $Co^{2+}/Co^{3+}/Co^{4+}$ and OH^- in the electrolyte.[35] Notably, the CV curves of P-Co_3O_4@P, N-C and Co_3O_4@N-C electrodes exhibit larger integral area than that of Co_3O_4, and P-Co_3O_4@P, N-C electrode possesses the largest enclosed CV area among these four electrodes. The increase in current density response of P-Co_3O_4@P, N-C electrode could be mainly ascribed to the heteroatom modulation as well as highly conductive carbon matrixes that synergistically increase the electrochemical activity.

To provide more detailed electrochemical properties of P-Co_3O_4@P, N-C, we conducted the CV curves at different scan rates (Figure 5b). With the increase of scan rate from 10 mV s^{-1} to 200 mV s^{-1}, the shapes of the CV curves change slightly, suggesting the highly reversible electrochemical behavior of P-Co_3O_4@P, N-C.

According to previous studies,[6a, 36] the current response (I) has a relationship with scan rate (v), which obeys the power law formula of $I = a \cdot v^b$ (where a is adjustable value, and b-value is the slope of $log(v) - log(I)$ plot).[37] Theoretically, the slope b assumes a value of 0.5 for complete diffusion-controlled behavior, whereas b = 1.0 presents complete capacitive response. The fitting slopes corresponding to the cathodic peaks of Co_3O_4, P-Co_3O_4, Co_3O_4@N-C, and P-Co_3O_4@P, N-C electrodes are ~0.789, 0.797, 0.845, and 0.856, respectively (Figure 5c), which are more close to 1, revealing their dominated "extrinsic" pseudocapacitive charge-storage properties.[6a, 6c-e, 38] The stored charge can be quantized using the formula $I = K_1V + K_2V^{1/2}$, where K_1V and $K_2V^{1/2}$ are charge contributions of the capacitive and diffusion-controlled Faradaic processes, respectively.[6a] The formula can also be converted into $\frac{I}{V^{1/2}} = K_1V^{1/2} + K_2$, where k_1 and k_2 are slope and intercept values determined from the linear plot between $\frac{I}{V^{1/2}}$ and $V^{1/2}$, respectively. The charge contribution fractions of the cathodic process of P-Co_3O_4@P, N-C at different scan rates are plotted (Figure S20). The contribution of capacitive process increases with the increasing scan rates and occupies prominent advantage of the whole charge at high scan rates. Even at a low scan rate of 10 mV s^{-1}, the capacitive contribution accounts for ~57.5%, illustrating the fast kinetics of P-Co_3O_4@P, N-C. These findings reveal that P introduction and defective carbon offer more effective pathways for ion transport to surface active sites. The dominant capacitive behavior of these samples can be ascribed to the rapid transfer of electrons and electrolyte ions, as well as the inhibition of the phase transformation in active

materials during charge storage,[39] which is consistent with reported Ni or Co oxides/hydroxides recently.[6, 8, 40]

Figure 5d shows the comparative GCD curves of Co_3O_4, P-Co_3O_4, Co_3O_4@N-C, and P-Co_3O_4@P, N-C electrodes at a discharge current density of 1 mA cm^{-2}. A small potential plateau is observed in all the GCD curves, which is due to the crystallographic phase transformation upon Faradaic charge-transfer processes.[6c, 6d, 6f] Evidently, the discharge time of the P-Co_3O_4@P, N-C electrode is longer than that of the other electrodes, which is consistent with the CV results. Based on the GCD curves (Figure S21), the specific capacities of Co_3O_4, P-Co_3O_4, Co_3O_4@N-C, and P-Co_3O_4@P, N-C electrodes at a current density of 1 mA cm^{-2} are found to be 225, 480, 351, and 669 mC cm^{-2}, respectively (Figure 5e). Such high specific capacity of P-Co_3O_4@P, N-C is also superior to those of commonly reported MOF-derived battery-type materials (Table S1). Surprisingly, the specific capacity of 513 mC cm^{-2} is retained for P-Co_3O_4@P, N-C electrode at a high current density of 30 mA cm^{-2}, whereas the specific capacity of Co_3O_4, P-Co_3O_4, and Co_3O_4@N-C electrodes decrease to 156, 345, and 264 mC cm^{-2}, respectively. The covalent–ionic bond character is a critical factor to evaluate the reaction kinetics of electrode materials. The character of chemical bonds can be determined using the equation (%)=$\exp[-0.25(X_c-X_a)^2]$,[28] where X_c and X_a present the electronegativity values of the cation and anion, respectively. Based on this equation, the covalent characters of Co–O and Co–P were 54.4% and 67.7%, respectively (X_{Co} = 1.88, X_O = 3.44, and X_P = 2.19). The high degree of covalency in

P-Co_3O_4@P, N-C implies the high energy of electrons in the 3d orbitals of Co,[28, 41] which provides more available electron carriers. Further, the average interatomic distance of Co–P (~2.26 Å) is larger than that of Co–O (~1.93 Å).[42] The increased covalency degree and bond distance arouse the decreased energy to attraction of the electrons in the 3d orbitals of Co^{2+} or Co^{3+} in P-Co_3O_4@P, N-C, thus decreasing the energy required to extract electrons during redox reactions[43] and improving the surface reactivity of P-Co_3O_4@P, N-C.

Electrochemical impedance spectroscopy (EIS) analysis was performed to investigate the enhanced reaction kinetics of P-Co_3O_4@P, N-C electrode. The Nyquist plots show the intercept of *x* axis corresponding to the serial resistance (R_s, the sum of the contact resistance, electrolyte resistance and electronic resistance of electroactive material and substrate),[9] whereas the small semicircle is related to the charge-transfer resistance (R_{ct}) associated with the redox reactions at the interface between the electrolyte and electrode.[4] The inclined line in the EIS curve at the low-frequency region signifies the Warburg resistance (R_w), which corresponds to the diffusion-limited and interfacial, nonequilibrium redox reactions.[26a] The EIS plot of P-Co_3O_4@P, N-C electrode presents smaller R_s (0.40 Ω) and R_{ct} (0.33 Ω) than those of Co_3O_4 (R_s= 0.91, R_{ct}= 0.54 Ω), P-Co_3O_4 (R_s= 0.74 Ω, R_{ct}= 0.40 Ω), and Co_3O_4@N-C (R_s=0.73 Ω, R_{ct}= 0.35 Ω) electrodes (Figure S22). Furthermore, the P-Co_3O_4@P, N-C electrode exhibits a straight line along imaginary axis with a higher slope than the other electrodes, implying the low R_w for fast ion diffusion between P-Co_3O_4@P, N-C and the electrolyte. These

findings indicate that P-Co_3O_4@P, N-C is more electrochemically active than the other electrodes due to the introduction of P atom and defect-rich carbon structure. The cycling stability was evaluated by repeating GCD measurements at a current density of 30 mA cm^{-2} (Figure 5f). After 5,000 cycles, the P-Co_3O_4@P, N-C electrode retains the specific capacity of 497 mC cm^{-2} (95.2% capacity retention), which is superior to that of Co_3O_4 (141 mC cm^{-2}), P-Co_3O_4 (348 mC cm^{-2}), and Co_3O_4@N-C (336 mC cm^{-2}) electrodes. Notably, the slight increase of the specific capacity of Co_3O_4@N-C electrode in the initial cycles could be ascribed to incomplete electro-activation of the electrode material.[44] Throughout the entire cycling test, all samples deliver high Coulombic efficiencies over ~96.2% (Figure S23), indicating their high electrochemical reversibility.[45] The SEM images of cycled P-Co_3O_4@P, N-C shows that the overall 1D morphology can be preserved (Figure S24a, b), indicating its excellent structural stability. The corresponding EDS elemental mapping further reveals the existence of Co, O, P, N, and C, implying that the incorporated heteroatoms are stable during the long-term cycling test (Figure S24c–i). The EIS plots of P-Co_3O_4@P, N-C electrode before and after cycling tests show a slight change, which supports the good electrochemical stability (Figure S25).

The excellent electrochemical performances of P-Co_3O_4@P, N-C electrode can be mainly attributed to the following merits (Figure S26): (1) Electroactive materials integrated on CF conductive substrate with chemically stable interface enables high electronic/ionic conductivity and provides high available surface area, thus ensuring

fast electrochemical kinetics and good structural stability. (2) After pyrolysis, the MOF-derived P-Co_3O_4@P, N-C encapsulated configuration with bridged bonds yields intimate contact between P-Co_3O_4 and defect-rich carbon and renders P-Co_3O_4 highly dispersed in the 1D carbon matrix, thereby greatly favoring fast electron transport and long-term cyclic durability. (3) The void pores existing in the P-Co_3O_4@P, N-C can accommodate structural expansion upon cycling and facilitate electrolyte ion diffusion into the electrode. (4) P-Co_3O_4@P, N-C hybrid has synergistic performance advantages of high specific capacity of Co_3O_4 and fast rate capability of carbon. (5) The incorporation of the heteroatom in P-Co_3O_4@P, N-C is anticipated to tune the electrical properties and provide more accessible electroactive sites for electrolyte ions, leading to more efficient pathways for fast electron/ion transport. Therefore, the distinct structural and electrical advantages of P-Co_3O_4@P, N-C are responsible for fast reaction kinetics, thus showing the excellent electrochemical behavior.

2.3 Density functional theory (DFT) calculations

In order to disclose the underlying effect of P dopants on enhanced elelctrochemical activity of P-Co_3O_4 and P, N-C, we conducted the DFT calculations. The crystal structures and the density of states (DOS) of the bulks Co_3O_4 and P-Co_3O_4 are shown in Figure S27 and **Figure 6**a, respectivily. When a P atom is introduced into the bulk Co_3O_4, a doping energy level generates in the band gap near the Fermi level and band gap decreases from 1.38 eV to 1.17 eV. Meanwhile, as a P atom is introduced into the N-C, the electronic state moves to the negative direction (Figure 6b). Decrease of the

band gap and change of the electronic state faciliate the excitation of more charge carriers to the conduction band for fast Faradaic reaction, which are consistent with EIS plots (Figure S22).

The adsorption free energy of OH^- (ΔE_{OH*}) in the electrolyte on optimized surfaces of the active materials is a key factor in evaluating the Faradaic reaction kinetics.[41] The ΔE_{OH*} can be calculated as follows,[46]

$$\Delta E_{OH*} = E(OH*) - E(*) - (E_{H_2O} - 1/2E_{H_2}) \quad (1)$$

where E(OH*), E(*) are the total energy of the OH adsorbed structure and the structure without OH adsorption, respectively. E_{H_2O} and E_{H_2} are the chemical potentials of the H_2O and H_2, respectively, in the DFT calculation. The adsorption of OH^- on the optimized surfaces of Co_3O_4 (110), P-Co_3O_4 (110), N-C and P, N-C (Figure S28) is explored. As shown in Figure S29, two adsorption sites (I and II) are selected for (110) surface of Co_3O_4 and P-Co_3O_4. The (110) surface of P-Co_3O_4 shows a reduced OH^- adsorption energy compared with that of Co_3O_4 (Figure 6c–f and Table S3), demonstrating that the Faradaic reaction involving with OH^- state would more easily to take place on the surface of active materials after P doping, leading to accelerated reaction kinetics. As shown in Figure S30a, b, two adsorption sites (I and II) are selected for N-C and P, N-C, respectively. Due to P atom doped in N-C, the ΔE_{OH*} is highly reduced (Figure 6g–j and Table S2), revealing that the P, N-C has a stronger capability of adsorbing OH^-.

The reduced ΔE_{OH*} on P-Co_3O_4 and N-C are due to the charge density redistribution and the change of the electronic states generates by the P dopant. To reveal the effect of P dopant on the electronic structure of Co_3O_4, the charge density difference between the doped and undoped structures was calculated (Figure 6k). The charge transfer occurs mainly between P atom and neighboring Co atoms. Meanwhile, Bader charge analysis (Figure S30c, d) on N-C and P doped N-C also supports the change of ΔE_{OH*}. The bader charge on the carbon atom (adsorption site I of Figure S30d) around P atom increases (~0.02) compared with that on the N-C, indicating that the electron can transfer from the carbon atom to its neigboring atoms due to the P dopant. The adsorption site I has more positive charge, which helps bond with OH^-. For the adsorption site II, although the bader charge of the carbon atom decreases a little bit (~0.05), the energy level of the bonding orbital between the adsorption site C and site O in adsorbed OH^- radical shifts to more negative energy level after introducing P dopant (Figure S31), which contributes to the adsorption of OH^-. Our simulation-results agree well with the experimental data observations and verify the positive effect of P dopants in P-Co_3O_4@P, N-C for enhanced electrochemical reactivity.

2.4 Characterization and charge storage properties of negative electrode materials

The typical FESEM images of Co@P, N-C are shown in Figure S32a−c, from which the Co@P, N-C well preserves the structural architecture of Co@N-C except that the surface of nanowires become rough. The SEM-EDS spectrum shows that the Co@P, N-C contains Co, P, N, and C (Figure S32d–i). The content of Co nanoparticles is 38.89

wt% in the Co@P, N-C based on EDS analysis (Figure S32j). The TEM image of the Co@P, N-C further reveals its nanowire structure embedded with Co nanoparticles (Figure S33a–c). The lattice fringes of 0.208 and 0.179 nm in the HRTEM image correspond to the (111) and (200) planes of metallic Co phase, respectively (Figure S33d). Considering that N, P, and C are uniformly distributed in the whole nanowire, the STEM-EDS presents that Co has a distinct contrast along the edge to the center (Figure S33e–i), indicating the successful formation of Co nanoparticles confined within the carbon framework. The encapsulated metallic nanoparticles possess a strong coupling with graphitic carbon matrix, from which metal electrons can transfer to carbon freely and tune electronic properties, thus ensuring fast electrochemical reaction kinetics of electrode materials.[12] For a systematic comparison, the structure and composition of the Co@N-C were verified using SEM and corresponding EDS mapping analyses (Figure S34). XRD results show that the diffraction peaks of Co@P, N-C are well indexed to the phase of face-centered cubic Co (PDF No. 89−4307), which show no obvious changes as compared with Co@C and Co@N-C (Figure S35a). Hence, no phase/structural transition occurs during phosphorization. The influence of P on structural defects can be confirmed based on the ratio of I_D/I_G in the Raman spectra (Figure S35b), where the relative intensity ratio of I_D/I_G for Co@P, N-C (1.11) is higher than those of Co@C (0.97) and Co@N-C (1.06). Analysis of the N 1s and P 2p XPS spectra of Co@P, N-C also supports the successful incorporation of N and P within the carbon structure (Figure S36). These findings are also in accordance with the DFT results (Figures 6i and 6g−j).

The CV curves of the Co@C, Co@N-C and Co@P, N-C electrodes at a scan rate of 50 mV s^{-1} are displayed in Figure S37a. Clearly, the integrated area of the CV curve for Co@P, N-C electrode is larger than those of Co@C and Co@N-C, suggesting the superior electrochemical activity of Co@P, N-C. The CV curves of Co@P, N-C present a quasi-rectangular shape at the scan rates ranging from 10 to 200 mV s^{-1} (Figure S37b), revealing its good capacitive characteristic. This feature is further verified by the GCD profiles of Co@P, N-C, which present nearly symmetrical triangle shapes at different current densities (Figure S37c). Furthermore, Co@P, N-C also delivers a longer discharge time than Co@C and Co@N-C at the current density of 1 mA cm^{-2} (Figure S37d), matching well with the CV results. The specific capacitance of Co@P, N-C electrodes is 353 mF cm^{-2} at 1 mA cm^{-2} (Figure S37e), which is superior to those of Co@C (130 mF cm^{-2}) and Co@N-C (178 mF cm^{-2}) as well as previously reported carbon materials (Table S3). Notably, after a 30-fold increment in the current density, Co@P, N-C electrode retains 80.6% of its original value with a favorable capacitance of 284 mF cm^{-2} even at a high current density of 30 mA cm^{-2}, which is much higher than those of Co@C (46.2%) and Co@N-C (68.8%). Moreover, this Co@P, N-C electrode shows an impressive electrochemical stability with ~96.0% retention of the initial capacitance after 10 000 cycles at 30 mA cm^{-2} (Figure S37f). By contrast, the Co@C and Co@N-C electrodes only remain 80% and 92.1%, respectively. The superior electrode kinetics of Co@P, N-C in electrochemical reactions can be validated by the obtained Nyquist plot (Figure S38) in which R_s and R_{ct} are 0.97 and 0.59 Ω,

respectively. For comparison, the EIS plots of Co@N-C (R_s=1.51 Ω; R_{ct}=0.94 Ω) and Co@N-C (R_s=1.42 Ω; R_{ct}=0.82 Ω) electrodes display obvious increase of R_s and R_{ct}. The reduced internal resistance and enhanced charge transfer kinetics of Co@P, N-C are due to the modified polarity and tuned electron distribution of adjacent carbon atoms after N/P doping ,[17b, 26a] which thus facilitates high electronic conductivity and increased electrolyte ion penetration into the materials. As shown in Figure S39, the overall morphology of cycled Co@P, N-C is maintained without obvious agglomeration. The change is probably due to cyclic stress, caused by volumetric expansion and shrinking upon the succeeding GCD process. After cycling test, the EIS plot of Co@P, N-C electrode exhibits slight changes, but the R_{ct} of the Co@C and Co@N-C electrodes increases largely (Figure S40), indicating the high cycling stability of Co@P, N-C electrode. These findings reveal that N and P heteroatom dopants could change the electron features of carbon for enhanced capacitive property, which is well consistent with theoretical results (Figures 6b and 6g–j).

2.5. Electrochemical properties of flexible quasi-solid-state P-Co_3O_4@P, N-C//Co@P, N-C ASCs

To evaluate the potential of the electrode materials in actual application, we assembled flexible quasi-solid-state ASCs by using the P-Co_3O_4@P, N-C as the positive electrode material, Co@P, N-C as a negative electrode material, and polyvinyl alcohol (PVA)/KOH as gel electrolyte, together with a piece of cellulose separator paper (**Figure 7**a). For an ASC device, the positive and negative electrodes should follow the

charge balance relationship of $q^+ = q^-$.[3] Accordingly, the optimal mass ratio of the positive electrode material to the negative electrode material is determined to be 1:0.49 in the devices based on the comparative CV results of two electrodes at 20 mV s^{-1} (Figure S41a). The assembled ASC devices can integrate the complementary potential windows of P-Co_3O_4@P, N-C and Co@P, N-C. A sequence of CV curves of the P-Co_3O_4@P, N-C//Co@P, N-C ASC device in different voltage windows at a scan rate of 20 mV s^{-1} confirm that it can successfully operate at 1.5 V (Figure 7b). All the CV curves at various scan rates exhibit quasi-rectangular shape and nearly symmetric feature (Figure 7c), indicating the remarkable reversibility and excellent electrochemical characteristics of the device. Figure 7d shows that the CV curves of two devices connected in parallel displays an almost two times larger integral area than that of the single device at 20 mV s^{-1}. Furthermore, three such devices coupled in series can generate an operating voltage of 0−4.5 V and deliver CV curves that are similar in shape compared with an individual device, indicating their outstanding electrochemical performance uniformity.

The GCD curves of the P-Co_3O_4@P, N-C//Co@P, N-C ASC device at different current densities display an approximate linear response between the operating voltage and charging/discharging time (Figure 7e), confirming its good capacitive behavior. By connecting three ASC devices in series, the overall operating voltage window is quadrupled with only slight capacitance degradation (Figure 7f). Furthermore, the discharge time of two such parallel devices is almost doubled compared with the single

device, illustrating their good performance stability. Based on the total mass loadings of the positive and negative electrode materials, high specific capacitance of 152.4 F g^{-1} is obtained at a current density of 1 A g^{-1}, which can be retained at 76.0 F g^{-1} at a high current density of 15 A g^{-1} (Figure S41b). The power and energy densities of the ASC device were calculated based on the discharge curves, as presented in the Ragone plot (Figure 7g). The device shows an energy density of 47.6 Wh kg^{-1} at a power density of 750 W kg^{-1}. Notably, the P-Co_3O_4@P, N-C//Co@P, N-C device exhibits an energy density of 23.8 Wh kg^{-1} even at a high power density of 11,250 W kg^{-1} (equivalent to a discharge time of 7.6 s), indicating the fast rate capability of the assembled device. The attained energy and power densities of our device exceed those of recently reported ASC devices by using Co−based or MOF-derived nanostructures as electrode materials, such as Co_3O_4@N-doped carbon (N-C)//AC,[26a] Co_3O_4@reduced graphene oxide (rGO)//AC,[47] Co_3O_4//AC,[35] CoNi-MOF//AC,[2f] MOF-derived $NiCo_2S_4$//AC,[48] and NiCoP/NiCo-OH//MOF-derived carbon.[49] The Nyquist plot (Figure S41c) shows that our assembled ASC device has a low R_s (1.7 Ω) and R_{ct} (23.2 Ω), which provide rapid electronic/ionic transport and ensured fast charging/discharging kinetics. The ASC device also delivers high Coulombic efficiency above 97.8% and excellent cycling stability with a capacitance retention of 92.9% after 5,000 GCD cycles at a current density of 15 A g^{-1} (Figure 7h). After cycling, the R_s and R_{ct} slightly change, which further indicates the good cycling stability. As a proof of concept, two ASC devices with tandem connection could readily power a light-emitting diode (LED, ~2 V) indicator (Inset of Figure 7h). To evaluate the electrochemical performance of the ASC

devices under mechanical strain, we performed the CV curves at different bending angles (Figure S42). Prominently, Figure 7i shows that all the CV curves remain almost coincident without evident capacitance fluctuation (less than 4.8%), implying the good mechanical flexibility of the ASC device. Furthermore, the device retains 85.3% of its original capacitance at 20 mV s^{-1} even after bending from 0° to 90° for 500 cycles (Figure S41d). These results impart great potential to apply the as-constructed ASC devices in flexible high-power energy storage systems with desirable energy density.

3. Conclusion

In summary, we have successfully designed the in situ transformed 1D Co−MOF as a novel precursor to in situ synthesize P-Co_3O_4@P, N-C hybrid structure on the CF substrate through a pyrolysis–oxidation–phosphorization strategy. Such favorable P-Co_3O_4@P, N-C architecture prevents structural agglomeration and provides abundant electroactive sites/nanovoids/surface defects, modified electrical properties and tuned covalent bond characteristics of cobalt species. Theoretical results reveal that the P dopants simultaneously reduce the adsorption barrier of OH^- and regulate the electron conduction of P-Co_3O_4 and P, N-C. These properties enable accelerated charge/mass transfer kinetics of P-Co_3O_4@P, N-C, which thus delivers a high specific capacity of 669 mC cm^{-2} at 1 mA cm^{-2}, superior rate capability (76.7% capacity retention at 30 mA cm^{-2}) and impressive cycling stability. Flexible ASC devices can be readily assembled using P-Co_3O_4@P, N-C and Co@P, N-C, which exhibit an energy density of 47.6 W h kg^{-1} at a power density of 750 W kg^{-1}, high cycling stability and excellent

mechanical flexibility with light capacitance change under different bending angles. This design concept proposed here may provide insights into the construction of other new type MOF-derived hybrids with high energy and power densities for flexible electronics.

Conflict of interest

There are no conflicts to declare.

Acknowledgements

This research was partially supported by the Nanomaterial Technology Development Program (NRF-2017M3A7B4041987) and Korean Government (MSIP) (Grant No. 2015R1A5A1037668).

Graphical abstract

We firstly report a hybrid structure of P-doped Co_3O_4 (P-Co_3O_4) ultrafine nanoparticles in situ encapsulated into P, N co-doped carbon (P, N-C) nanowires by a pyrolysis-oxidation-phosphorization of 1D metal–organic framework derived from Co-layered double hydroxide as self-template and reactant. This hybrid provides strong intercomponent synergy, increases availability of active sites/interfaces and improves the electron/ion transfer, giving rise to high electrochemical reactivity. Theoretical calculations reveal that the P dopants could reduce the adsorption barrier of OH^- and regulate the electron conduction of P-Co_3O_4@P, N-C. Accordingly, more "extrinsic" pseudocapacitance occurs on the surface or near the surface of electroactive material. The resultant P-Co_3O_4@P, N-C exhibited a high specific capacity, excellent rate performance (76.7% retention after 30-fold increase in current density), while retaining specific capacity of 95.2% over 5,000 cycles at 30 mA cm^{-2}. The assembled quasi-solid-state ASC devices with P-Co_3O_4@P, N-C and Co@P, N-C elelctrode materials achieved a high energy density of 47.6 W h kg^{-1} at a high power density of up to 750 W kg^{-1} along with excellent flexibility. This ingenious strategy can effectively regulate the reaction kinetics of electrode materials and further inspire more research in the field of electrochemical storage systems.

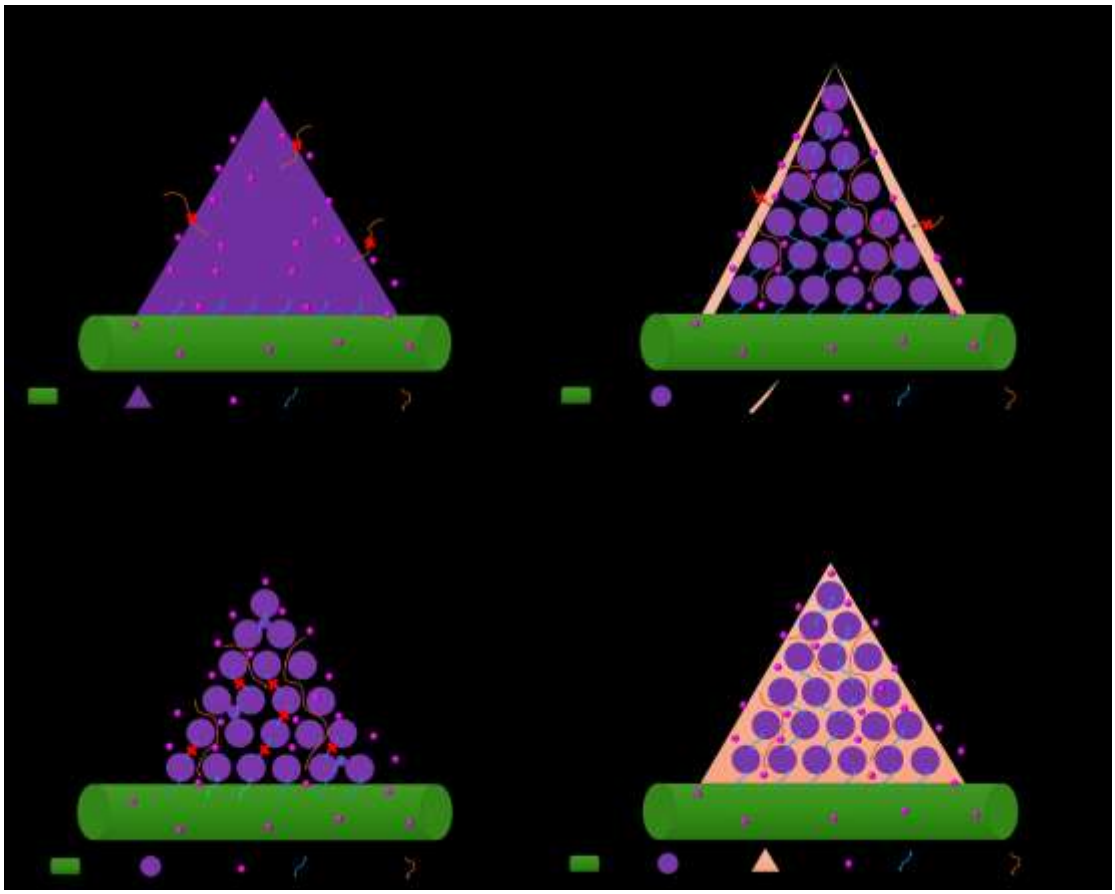

Figure 1. Schematic of various strategies to tune the structural configuration of electroactive materials for fast electron transfer and rapid electrolyte ion diffusion in supercapacitors: (a) microsized electroactive particles, (b) nanosized electroactive particles, (c) nanosized electroactive particle/surface coated carbon hybrids, and (d) highly oriented MOF-derived carbon matrix/nanosized electroactive particle hybrids deposited on substrate. The Red Cross on the arrows presents the charge transfer pathways with obstacles.

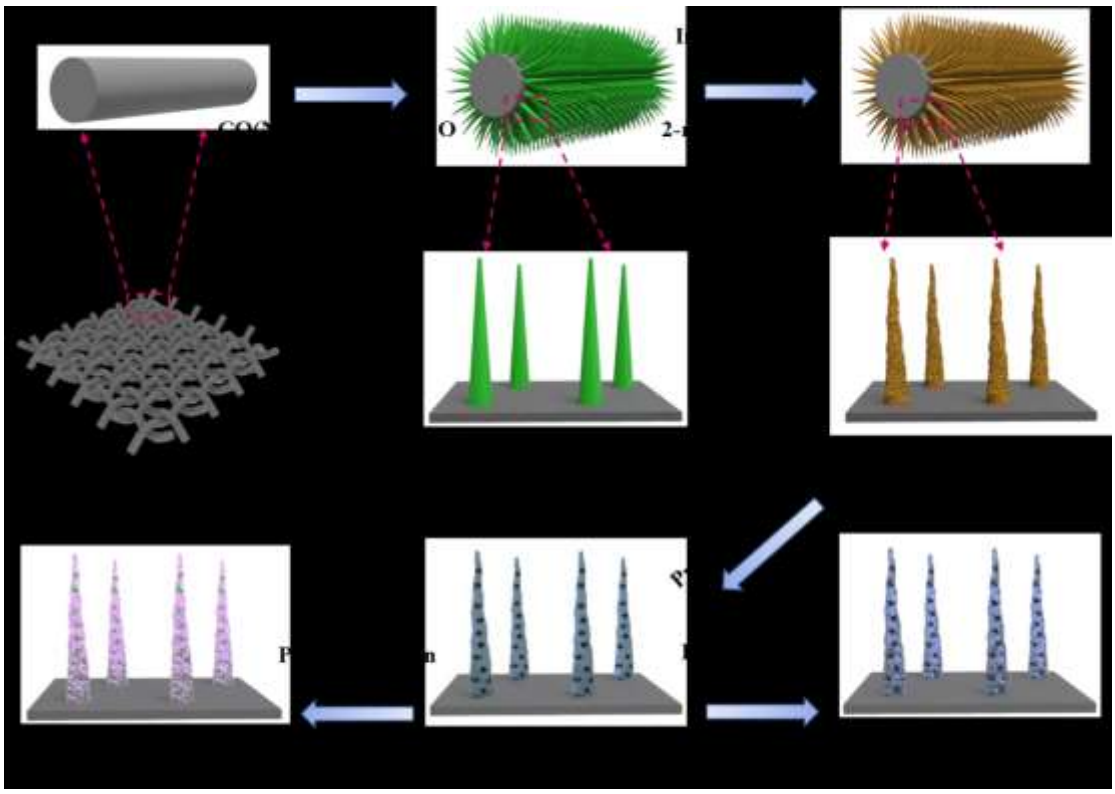

Figure 2. Schematic of the fabrication of the P-Co_3O_4@P, N-C and Co@P, N-C nanowires on CF substrate.

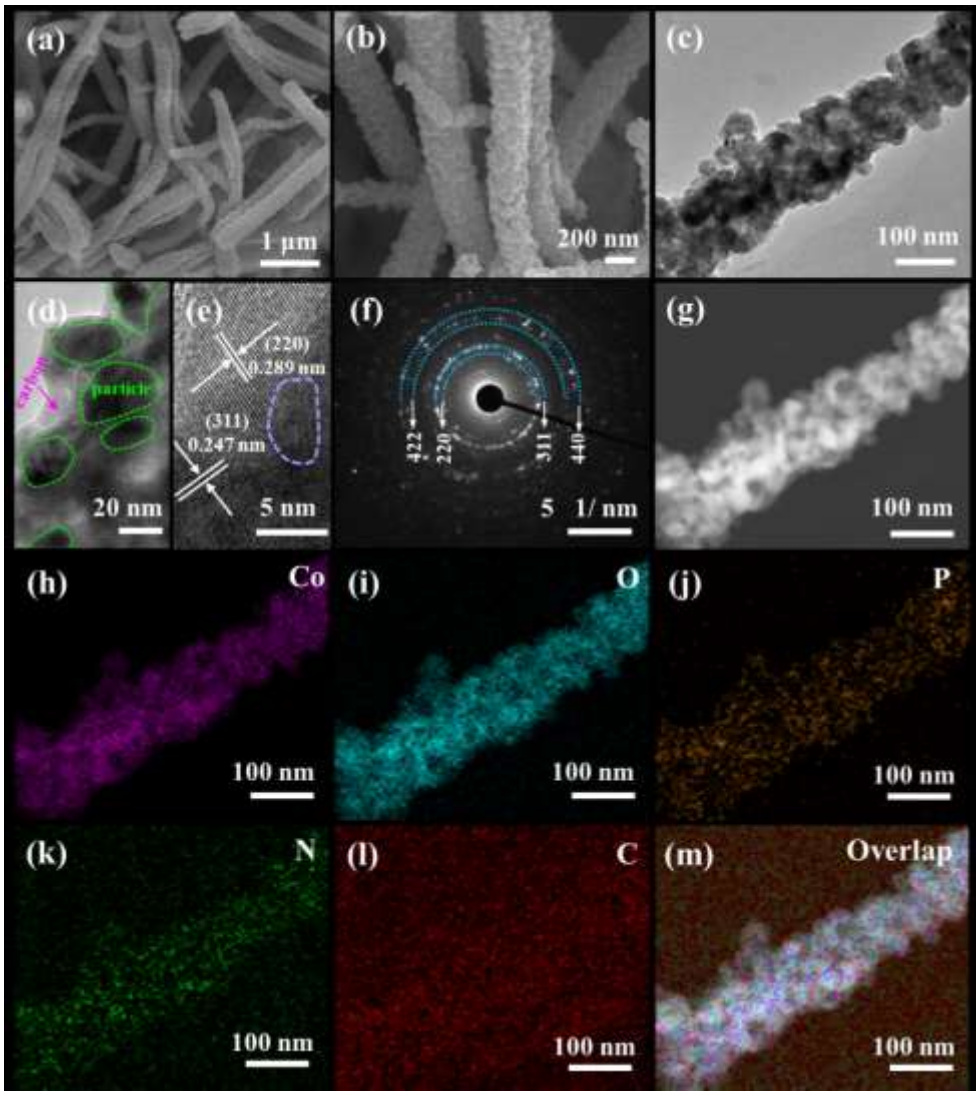

Figure 3. (a, b) SEM images, (c, d) TEM images, (e) HRTEM image, (f) SAED pattern, (g) STEM image, and (h–m) corresponding distributions of elemental Co, O, P, N, and C for P-Co_3O_4@P, N-C nanowires.

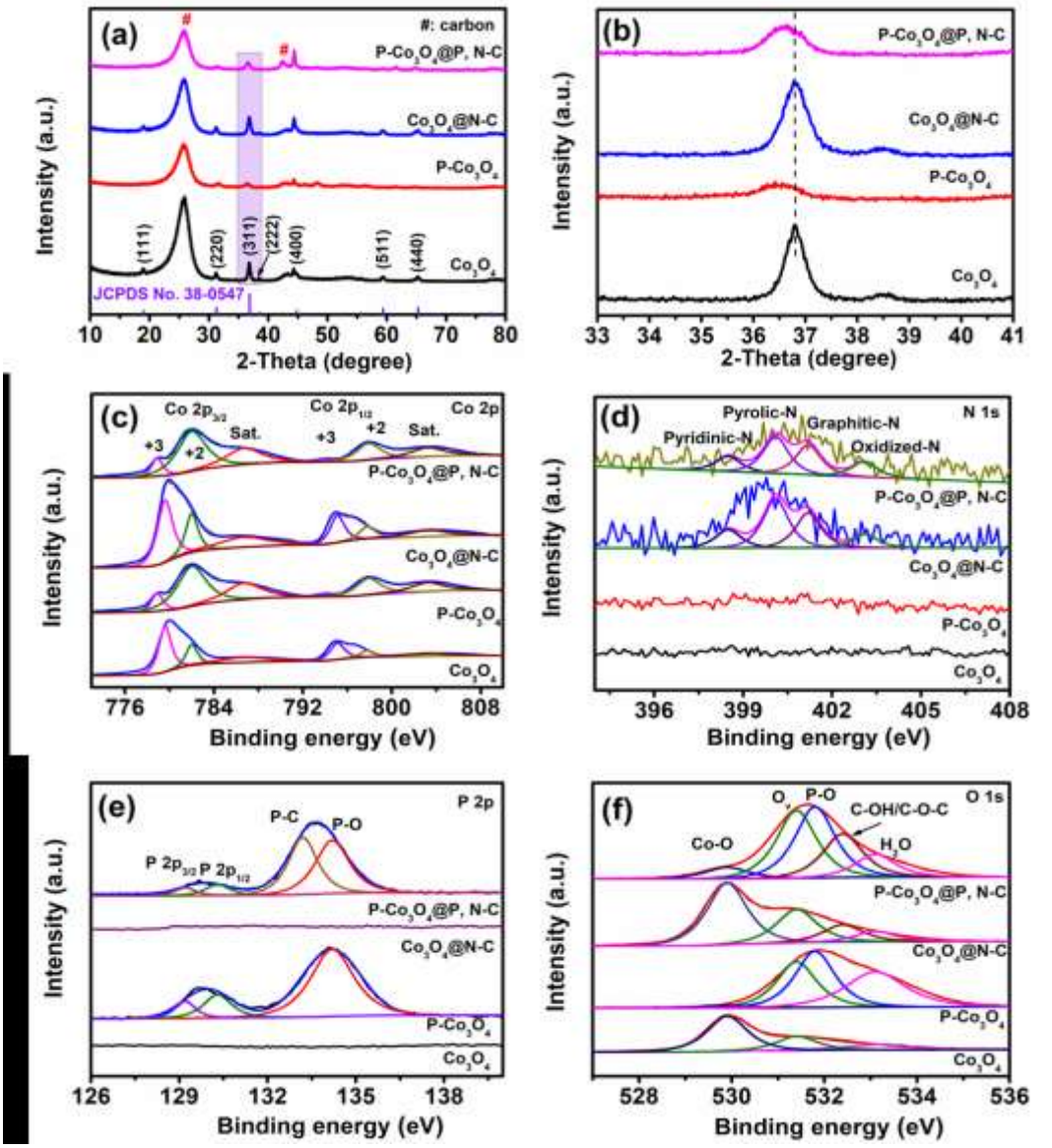

Figure 4. (a) XRD patterns, (b) amplified section in the (311) diffraction peak position, and high-resolution XPS spectra of (c) Co 2p, (d) N 1s, (e) P 2p, and (f) O 1s for Co_3O_4, P-Co_3O_4, Co_3O_4@N-C, and P-Co_3O_4@P, N-C nanowires.

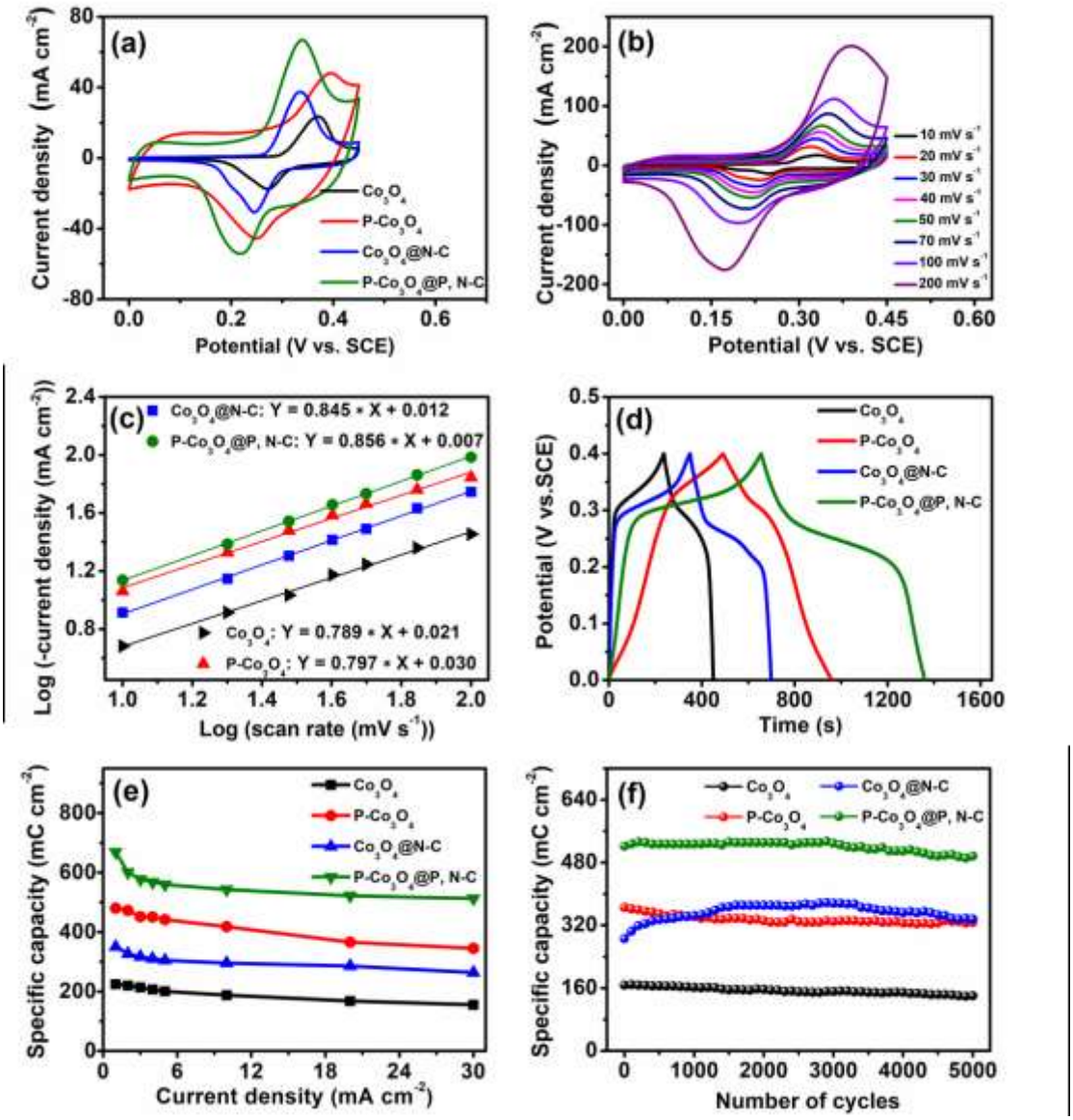

Figure 5. (a) Comparative CV curves of Co_3O_4, P-Co_3O_4, Co_3O_4@N-C, and P-Co_3O_4@P, N-C electrodes at 50 mV s^{-1}. (b) CV curves of P-Co_3O_4@P, N-C electrode at different scan rates. (c) Linear fitting of the cathodic peak current density versus the scan rate based on the CV curves of Co_3O_4, P-Co_3O_4, Co_3O_4@N-C, and P-Co_3O_4@P, N-C electrodes. (d) Comparative GCD profiles of Co_3O_4, P-Co_3O_4, Co_3O_4@N-C, and P-Co_3O_4@P, N-C electrodes at 1 mA cm^{-2}. (e) Specific capacity plotted against current density. (f) Cycling performance at 30 mA cm^{-2}.

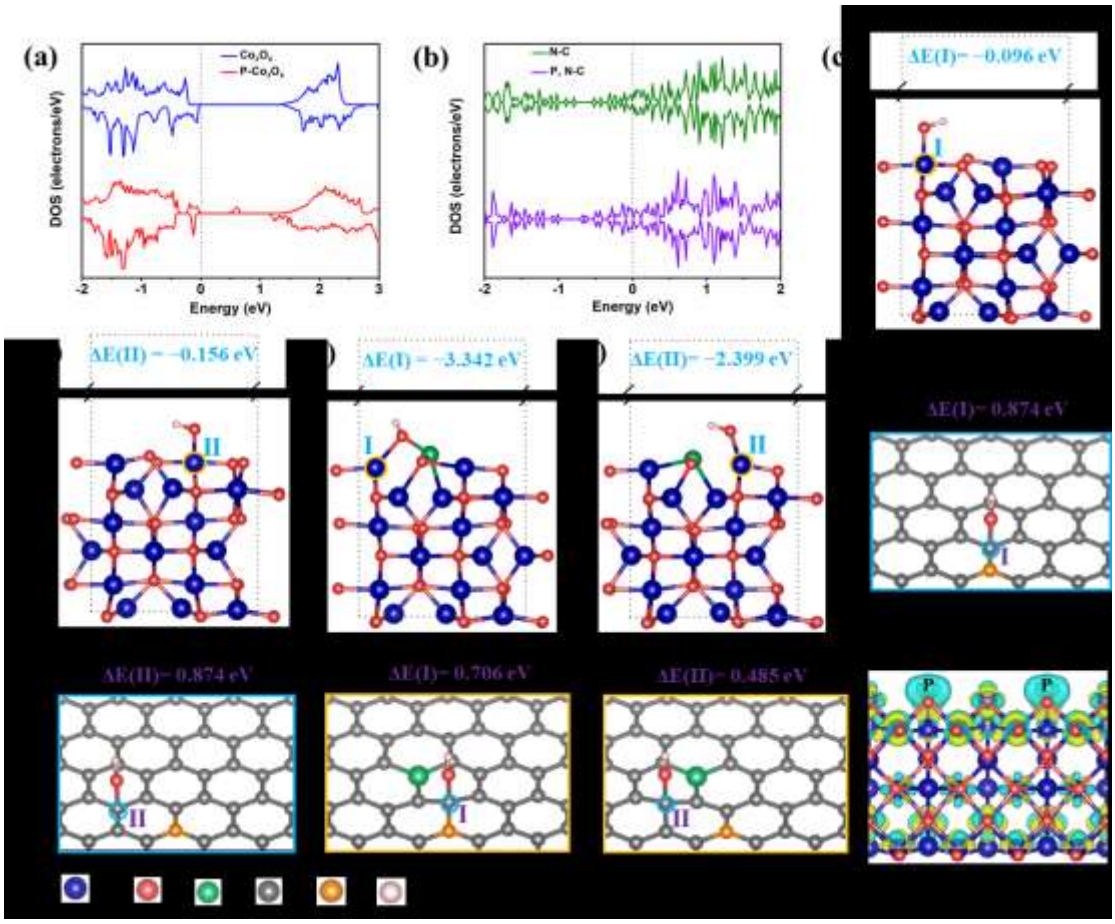

Figure 6. (a) Density of states (DOS) diagrams of bulk Co_3O_4 and P-Co_3O_4, (b) DOS diagrams of N-C and P, N-C. Adsorption sites (I and II) and ΔE_{OH*} of (c, d) Co_3O_4 (110), (e, f) P-Co_3O_4 (110) surface, (g, h) N-C and (i, j) P, N-C. (k) The charge density difference isosurfaces of P-Co_3O_4 (110) surfaces (the yellow and blue isosurfaces with isovalues of 0.01 eV/Å^3 represent increased and decreased charge density respectively).

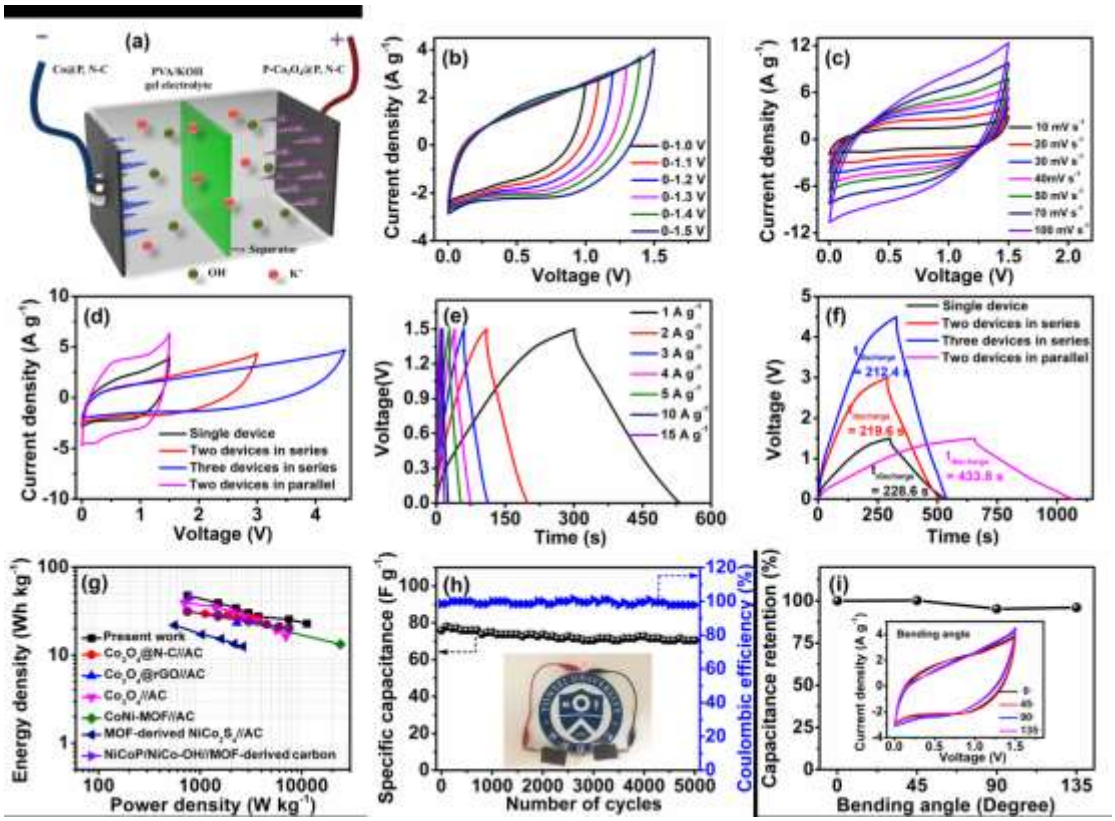

Figure 7. (a) Schematic of the assembled P-Co_3O_4@P, N-C//Co@P, N-C ASC device. (b) CV curves of the ASC device in different voltage windows at 20 mV s^{-1}. (c) CV curves of ASC device at different scan rates. (d) CV curves of the ASC devices connected in series and parallel. (e) GCD curves of the ASC device at different current densities. (f) GCD curves of the ASC devices connected in series and parallel. (g) Cycling performance and Coulombic efficiency as determined at 15 A g^{-1}; Inset shows the photograph of a red LED powered by two ASC devices connected in series. (h) Comparison of the Ragone plot of as-prepared ASC device and recently reported ASC devices. (i) Capacitance retention of the ASC device bent at different angles; Inset shows the CV curves at 20 mV s^{-1} under different bending states.

Reference

[1] a) L. Yao, Q. Wu, P. Zhang, J. Zhang, D. Wang, Y. Li, X. Ren, H. Mi, L. Deng, Z. Zheng, *Adv. Mater.* **2018**, 30, 1706054; b) J.-Q. Xie, Y.-Q. Ji, J.-H. Kang, J.-L. Sheng, D.-S. Mao, X.-Z. Fu, R. Sun, C.-P. Wong, *Energy Environ. Sci.* **2019**, 12, 194; c) X. Shi, S. Pei, F. Zhou, W. Ren, H.-M. Cheng, Z.-S. Wu, X. Bao, *Energy Environ. Sci.* **2019**, 12, 1534.

[2] a) P. Zhang, Y. Li, G. Wang, F. Wang, S. Yang, F. Zhu, X. Zhuang, O. G. Schmidt, X. Feng, *Adv. Mater.* **2019**, 31, 1806005; b) D. Zhao, W. Chang, C. Lu, C. Yang, K. Jiang, X. Chang, H. Lin, F. Zhang, S. Han, Z. Hou, *Small* **2019**, DOI: 10.1002/smll.201901494; c) P. Zhang, J. Wang, W. Sheng, F. Wang, J. Zhang, F. Zhu, X. Zhuang, R. Jordan, O. G. Schmidt, X. Feng, *Energy Environ. Sci.* **2018**, 11, 1717; d) P. Zhang, F. Wang, M. Yu, X. Zhuang, X. Feng, *Chem. Soc. Rev.* **2018**, 47, 7426; e) D. Sheberla, J. C. Bachman, J. S. Elias, C.-J. Sun, Y. Shao-Horn, M. Dincă, *Nat. Mater.* **2016**, 16, 220; f) T. Deng, Y. Lu, W. Zhang, M. Sui, X. Shi, D. Wang, W. Zheng, *Adv. Energy Mater.* **2018**, 8, 1702294; g) C. Zheng, J. Zhu, C. Yang, C. Lu, Z. Chen, X. Zhuang, *Sci. China Chem.* **2019**, 1; h) J. Zhu, C. Yang, C. Lu, F. Zhang, Z. Yuan, X. Zhuang, *Acc. Chem. Res.* **2018**, 51, 3191.

[3] S. Liu, Y. Yin, K. S. Hui, K. N. Hui, S. C. Lee, S. C. Jun, *Adv. Sci.* **2018**, 5, 1800733.

[4] Z. Pan, J. Yang, Q. Zhang, M. Liu, Y. Hu, Z. Kou, N. Liu, X. Yang, X. Ding, H. Chen, *Adv. Energy Mater.* **2019**, 9, 1802753.

[5] Y. Zhang, Z. Zhang, Y. Tang, D. Jia, Y. Huang, W. Pang, Z. Guo, Z. Zhou, *Adv. Funct. Mater.* **2019**, 1807895.

[6] a) Y. Shao, M. F. El-Kady, J. Sun, Y. Li, Q. Zhang, M. Zhu, H. Wang, B. Dunn, R. B. Kaner, *Chem. Rev.* **2018**, 118, 9233; b) C. Zhao, C. Yu, M. Zhang, H. Huang, S. Li, X. Han, Z. Liu, J. Yang, W. Xiao, J. Liang, *Adv. Energy Mater.* **2017**, 7, 1602880 ; c) J. Liu, J. Wang, C. Xu, H. Jiang, C. Li, L. Zhang, J. Lin, Z. X. Shen, *Adv. Sci.* **2018**, 5, 1700322; d) B. Zhao, D. Chen, X. Xiong, B. Song, R. Hu, Q. Zhang, B. H. Rainwater, G. H. Waller, D. Zhen, Y. Ding, *Energy Storage Mater.* **2017**, 7, 32; e) J. Sun, C. Wu, X. Sun, H. Hu, C. Zhi, L. Hou, C. Yuan, *J. Mater. Chem. A* **2017**, 5, 9443; f) J. Li, Z. Liu, L. Li, C. Zhu, D. Hu, *J. Electrochem. Soc.* **2016**, 163, A417.

[7] a) H. Wang, M. Wang, Y. Tang, *Energy Storage Mater.* **2018**, 13, 1; b) S. Peng, L. Li, H. B. Wu, S. Madhavi, X. W. D. Lou, *Adv. Energy Mater.* **2015**, 5, 1401172.

[8] M. Okubo, E. Hosono, J. Kim, M. Enomoto, N. Kojima, T. Kudo, H. Zhou, I. Honma, *J. Am. Chem. Soc.* **2007**, 129, 7444.

[9] J. Zhao, Z. Li, X. Yuan, Z. Yang, M. Zhang, A. Meng, Q. Li, *Adv. Energy Mater.* **2018**, 8, 1702787.

[10] R. Li, Y. Wang, C. Zhou, C. Wang, X. Ba, Y. Li, X. Huang, J. Liu, *Adv. Funct. Mater.* **2015**, 25, 5384.

[11] G. Cai, W. Zhang, L. Jiao, S.-H. Yu, H.-L. Jiang, *Chem* **2017**, 2, 791.

[12] C. Yan, Y. Zhu, Z. Fang, C. Lv, X. Zhou, G. Chen, G. Yu, *Adv. Energy Mater.* **2018**, 8, 1800762.
[13] W. Fu, E. Zhao, X. Ren, A. Magasinski, G. Yushin, *Adv. Energy Mater.* **2018**, 8, 1703454.
[14] a) Z. Zhang, Y. Zhu, Y. Zhong, W. Zhou, Z. Shao, *Adv. Energy Mater.* **2017**, 7, 1700242; b) S. Liu, Y. Yin, D. Ni, K. San Hui, K. N. Hui, S. Lee, C.-Y. Ouyang, S. C. Jun, *Energy Storage Mater.* **2018**, 19, 186.
[15] M. Yu, Z. Wang, C. Hou, Z. Wang, C. Liang, C. Zhao, Y. Tong, X. Lu, S. Yang, *Adv. Mater.* **2017**, 29, 1602868.
[16] Y. Zhang, S. Jiang, W. Song, P. Zhou, H. Ji, W. Ma, W. Hao, C. Chen, J. Zhao, *Energy Environ. Sci.* **2015**, 8, 1231.
[17] a) J. Zhang, L. Qu, G. Shi, J. Liu, J. Chen, L. Dai, *Angew. Chem. Int. Ed.* **2016**, 55, 2230; b) H. Hou, L. Shao, Y. Zhang, G. Zou, J. Chen, X. Ji, *Adv. Sci.* **2017**, 4, 1600243.
[18] J. Lin, H. Wang, Y. Yan, X. Zheng, H. Jia, J. Qi, J. Cao, J. Tu, W. Fei, J. Feng, *J. Mater. Chem. A* **2018**, 6, 19151.
[19] D. Yu, L. Ge, B. Wu, L. Wu, H. Wang, T. Xu, *J. Mater. Chem. A* **2015**, 3, 16688.
[20] J. Yang, F. Zhang, H. Lu, X. Hong, H. Jiang, Y. Wu, Y. Li, *Angew. Chem. Int. Ed.* **2015**, 54, 10889.
[21] A. A. Ensafi, S. E. Moosavifard, B. Rezaei, S. K. Kaverlavani, *J. Mater. Chem. A* **2018**, 6, 10497.
[22] C. Yan, G. Chen, X. Zhou, J. Sun, C. Lv, *Adv. Funct. Mater.* **2016**, 26, 1428.
[23] C.-S. Cheng, M. Serizawa, H. Sakata, T. Hirayama, *Mater. Chem. Phys.* **1998**, 53, 225.
[24] X. Dong, H. Jin, R. Wang, J. Zhang, X. Feng, C. Yan, S. Chen, S. Wang, J. Wang, J. Lu, *Adv. Energy Mater.* **2018**, 8, 1702695.
[25] Z. Wang, H. Liu, R. Ge, X. Ren, J. Ren, D. Yang, L. Zhang, X. Sun, *ACS Catal.* **2018**, 8, 2236.
[26] a) T. Liu, L. Zhang, W. You, J. Yu, *Small* **2018**, 14, 1702407; b) G. Cheng, T. Kou, J. Zhang, C. Si, H. Gao, Z. Zhang, *Nano Energy* **2017**, 38, 155.
[27] H. Liang, A. N. Gandi, D. H. Anjum, X. Wang, U. Schwingenschlögl, H. N. Alshareef, *Nano Lett.* **2016**, 16, 7718.
[28] T. Zhai, L. Wan, S. Sun, Q. Chen, J. Sun, Q. Xia, H. Xia, *Adv. Mater.* **2017**, 29, 1604167.
[29] S. Wang, Z. Xiao, Y. Wang, Y. Huang, C. Dong, J. Ma, S. Shen, Y. Li, *Energy Environ. Sci.* **2017**, 10, 2563.
[30] T. Jiang, N. Yin, Z. Bai, P. Dai, X. Yu, M. Wu, G. Li, *Appl. Surf. Sci.* **2018**, 450, 219.
[31] S. Yang, Y. Liu, Y. Hao, X. Yang, W. A. Goddard, X. L. Zhang, B. Cao, *Adv. Sci.* **2018**, 5, 1700659.
[32] X. Chen, Y. Li, X. Pan, D. Cortie, X. Huang, Z. Yi, *Nat. Commun.* **2016**, 7, 12273.
[33] D. Das, K. K. Nanda, *Nano Energy* **2016**, 30, 303.

[34] C.-Z. Yuan, Y.-F. Jiang, Z. Wang, X. Xie, Z.-K. Yang, A. B. Yousaf, A.-W. Xu, *J. Mater. Chem. A* **2016**, 4, 8155.
[35] S. Liu, D. Ni, H.-F. Li, K. N. Hui, C.-Y. Ouyang, S. C. Jun, *J. Mater. Chem. A* **2018**, 6, 10674.
[36] P. Simon, Y. Gogotsi, B. Dunn, *Science* **2014**, 343, 1210.
[37] a) X. Xu, J. Liu, J. Liu, L. Ouyang, R. Hu, H. Wang, L. Yang, M. Zhu, *Adv. Funct. Mater.* **2018**, 28, 1707573; b) H. Wang, Z. Yu, M. F. El-Kady, M. Anderson, M. D. Kowal, M. Li, R. B. Kaner, *Energy Storage Mater.* **2019**, 19, 137.
[38] X. Yu, S. Yun, J. S. Yeon, P. Bhattacharya, L. Wang, S. W. Lee, X. Hu, H. S. Park, *Adv. Energy Mater.* **2018**, 8, 1702930.
[39] a) A. S. Arico, P. Bruce, B. Scrosati, J.-M. Tarascon, W. Van Schalkwijk, World Scientific **2011**, p. 148; b) L. Chen, Y. Jiao, Z. Li, Y. Gao, *Electrochim. Acta* **2019**, 299, 388.
[40] V. Augustyn, P. Simon, B. Dunn, *Energy Environ. Sci.* **2014**, 7, 1597.
[41] J. Li, Z. Liu, Q. Zhang, Y. Cheng, B. Zhao, S. Dai, H.-H. Wu, K. Zhang, D. Ding, Y. Wu, *Nano Energy* **2018**, 57, 22.
[42] a) D.-H. Ha, L. M. Moreau, C. R. Bealing, H. Zhang, R. G. Hennig, R. D. Robinson, *J. Mater. Chem.* **2011**, 21, 11498; b) P. Feng, X. Bu, G. D. Stucky, *Nature* **1997**, 388, 735.
[43] C. Liu, C. Zhang, H. Fu, X. Nan, G. Cao, *Adv. Energy Mater.* **2017**, 7, 1601127.
[44] A. Ramadoss, K.-N. Kang, H.-J. Ahn, S.-I. Kim, S.-T. Ryu, J.-H. Jang, *J. Mater. Chem. A* **2016**, 4, 4718.
[45] H. Chen, Z. Shen, Z. Pan, Z. Kou, X. Liu, H. Zhang, Q. Gu, C. Guan, J. Wang, *Adv. Sci.* **2019**, 6, 1802002.
[46] a) M. Li, L. Zhang, Q. Xu, J. Niu, Z. Xia, *J. Catal.* **2014**, 314, 66; b) S. Li, C. Yu, Y. Yang, X. Song, S. Chen, L. Song, B. Qiu, J. Yang, H. Huang, W. Guo, *Small* **2018**, 14, 1803811; c) I. C. Man, H. Y. Su, F. Calle-Vallejo, H. A. Hansen, J. I. Martínez, N. G. Inoglu, J. Kitchin, T. F. Jaramillo, J. K. Nørskov, J. Rossmeisl, *ChemCatChem* **2011**, 3, 1159.
[47] M. Qorbani, T.-c. Chou, Y.-H. Lee, S. Samireddi, N. Naseri, A. Ganguly, A. Esfandiar, C.-H. Wang, L.-C. Chen, K.-H. Chen, *J. Mater. Chem. A* **2017**, 5, 12569.
[48] Y. Liu, Z. Wang, Y. Zhong, M. Tade, W. Zhou, Z. Shao, *Adv. Funct. Mater.* **2017**, 27, 1701229.
[49] X. Li, H. Wu, A. M. Elshahawy, L. Wang, S. J. Pennycook, C. Guan, J. Wang, *Adv. Funct. Mater.* **2018**, 28, 1800036.